Computational Particle Mechanics
https://doi.org/10.1007/s40571-023-00647-1

Analysis of cone-shaped projectile behavior during penetration into granular particles using the discrete element method

Hoo Min Lee[1] · Tae Hun Kim[1] · Gil Ho Yoon[1]

Received: 15 September 2022 / Revised: 28 June 2023 / Accepted: 16 August 2023

Abstract
In this study, the penetration behavior of a cone-shaped projectile into granular particles was analyzed using simulations based on the discrete element method (DEM). The rate-independent friction force and inertial drag force proportional to the squared projectile velocity are the principal force terms that interact between the projectile and the particles. Simulation results show that the friction force and inertial drag force follow the power law with respect to penetration depth and have changing tendencies before and after the complete penetration of the projectile into particles. Based on the results, a mathematical model is proposed to simplify the force terms using the penetration depth, projectile tip angle, and projectile length. The simplified force terms are physically explained using changes in the projectile–particle contact area and the fluidization of particles during dynamic collisions. Experiments were conducted using steel projectiles and ABS plastic beads to verify the accuracy of the mathematical model for real-life cases. The results of this study validate the proposed mathematical model of the rate-independent friction force and inertial drag force regarding the cone-shaped projectile behavior during penetration into granular particles.

Keywords Granular particle · Cone-shaped projectile · Discrete element method · Rate-independent friction force · Inertial drag force

1 Introduction

The present study analyzes the penetration behavior of a cone-shaped projectile into granular particles and proposes a mathematical model for the force terms involved in projectile penetration. The principal force terms during penetration are the rate-independent friction force and inertial drag force proportional to the squared projectile velocity. Discrete element method (DEM)-based simulations were conducted to consider inter-particle interactions during the penetration process. Based on the results, a mathematical model was proposed to simplify the force terms using the penetration depth, projectile tip angle, and projectile length. The simplified terms are physically explained using changes in the projectile−particle contact area and the fluidization of particles during dynamic collisions. Experiments were conducted using steel projectiles and ABS plastic beads to verify the accuracy of the proposed mathematical model.

The impact phenomena of objects on a granular bed can be found in various engineering cases and have been an important subject in terms of experiments and simulations. Relevant research on engineering applications has been done to evaluate contact models for agricultural granular materials [1], investigate track ballast−train wheel interaction [2], analyze track−soil traction [3], and model wet soil tillage processes [4]. To understand the statistical phenomena involved with the principle force terms and predict the complex and random nature of granular particles, studies have considered the static friction force between particles and objects in contact [5–9]. Studies have also been conducted on inertial drag and energy dissipation phenomena during the collision of objects with particles [10–13]. Based on the analyses of the principal force terms, various studies have been conducted to investigate the factors affecting the penetration behavior of projectiles. In [14], projectiles with various heads

✉ Gil Ho Yoon
ghy@hanyang.ac.kr

Hoo Min Lee
hoominlee95@gmail.com

Tae Hun Kim
woongpapa4@gmail.com

[1] School of Mechanical Engineering, Hanyang University, Seoul 04763, South Korea

Published online: 01 September 2023

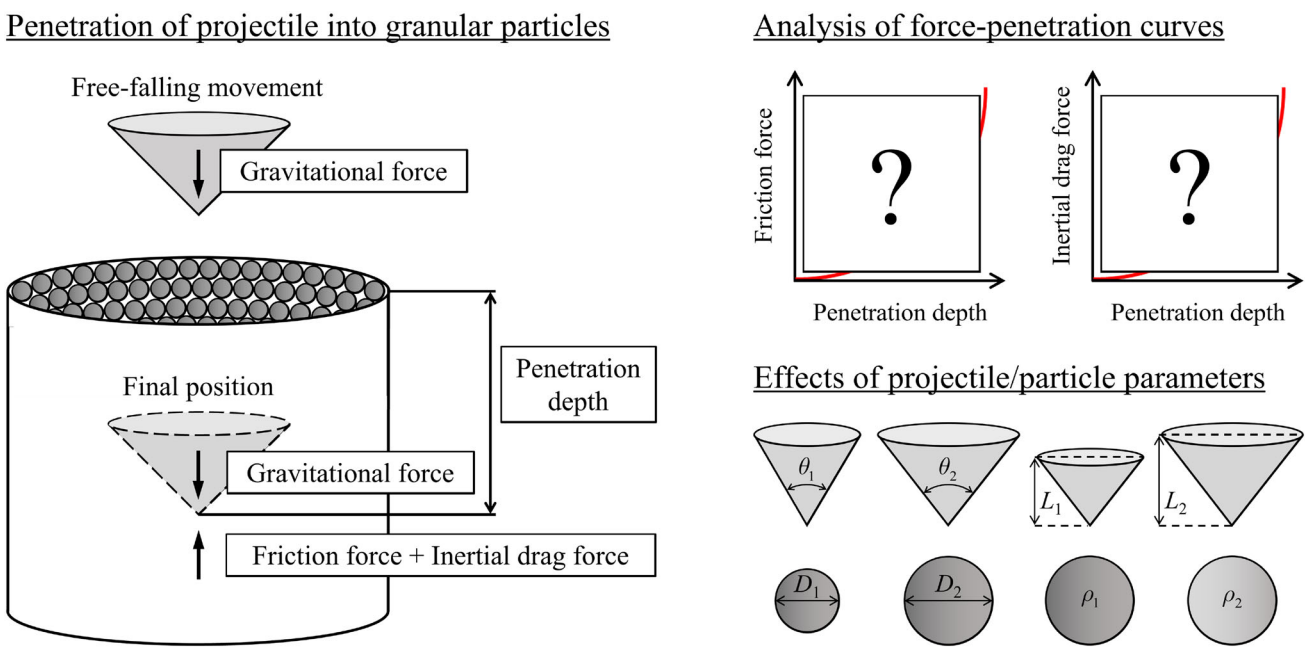

Fig. 1 Investigation of cone-shaped projectile behavior during penetration into granular particles

were considered to evaluate the effect of projectile density on particle penetration. Projectile geometry was considered in [15, 16] to investigate the shape dependence of the penetration of projectiles and the formation of impact craters. Analyses of the effects of moisture in granular beds [17] and irregular particle geometries [18] on penetration tendencies have also been conducted. Furthermore, research has been conducted to verify the effect of crater depth [19] and the wall effect [20] on projectile penetration. Using various factors affecting the penetration behavior, studies have been conducted to propose mathematical models related to the penetration processes into granular particles. The force law regarding the inertial drag force was proposed in [21], and the relationship between penetration depth and projectile drop distance was investigated in [22, 23]. The overall impact and penetration models for spherical and cylindrical projectiles were proposed and evaluated in [24–27]. Although relevant studies have been conducted to analyze the related force terms involved during penetration processes and suggest collision models for various penetration cases, limited studies have been conducted on cases of cone-shaped projectiles. Moreover, previous models have shown limitations in considering changes in penetration behaviors for different penetration stages, as evaluated in [28, 29]. They considered the entire penetration process using a single model. Thus, this study aims to analyze the cone-shaped projectile behavior during penetration into granular particles and propose a mathematical model for the fundamental force terms, considering the changes in behavior for different penetration stages.

The present study aims to analyze the penetration behavior of a cone-shaped projectile into granular particles, as shown in Fig. 1, and propose a mathematical model for the force terms associated with projectile penetration. The interaction force between the projectile and granular particles comprises a static friction force independent of the projectile velocity and an inertial drag force proportional to the squared projectile velocity. DEM-based simulations were conducted to acquire the friction force and inertial drag force data with respect to changes in the projectile penetration depth while considering the inter-particle interactions during the process. Considering the differences in velocity dependence, the friction force was computed using consistent penetration under quasi-static conditions, whereas the inertial drag force was computed using dynamic collision analysis. Projectiles of various tip angles and lengths were considered during the simulation to identify the effects of these parameters. A mathematical model was proposed based on the results to simplify the friction force and inertial drag force using the penetration depth, projectile tip angle, and projectile length. The changing tendencies before and after the complete penetration were also considered in the model. In addition, cases involving particles with various diameters and densities were conducted to verify that the penetration behavior remains consistent regardless of particle properties. The proposed model is physically explained using the changes in the projectile−particle contact area throughout the penetration process and fluidization of particles during dynamic collisions. Experiments were conducted for validation by

dropping steel projectiles onto ABS plastic beads. A high-speed camera and laser distance meter were used to track the projectile position at each observed time frame and measure the final penetration depth. The change in penetration depth over the penetration time period and maximum penetration depth values were acquired from the experiments. The experimental values were compared with the numerically calculated values using simplified force terms to validate the accuracy of the proposed mathematical model in real-life cases.

The remainder of this paper is organized as follows. Section 2 explains the penetration theory considering granular particles and the DEM method. Section 3 provides the background for the simulation setup and the numerical methodology for processing the force terms involved during projectile penetration. Section 4 presents an analysis of the simulation results to propose a mathematical model for force terms. Section 5 presents an experimental verification of the proposed model. Finally, conclusions are presented in Sect. 6.

2 Formulation

2.1 Penetration theory

The penetration theory that considers granular particles suggests a phenomenological model in which the interaction force between the projectile and granular particles comprises a static friction force independent of the projectile velocity and an inertial drag force proportional to the squared projectile velocity. Thus, the total drag force exerted on a penetrating projectile can be formulated based on the phenomenological model [24, 25] as follows:

$$F_d = f(z) + h(z)v^2 \tag{1}$$

where F_d, $f(z)$, and $h(z)v^2$ denote the total drag force exerted on the penetrating projectile, friction force, and inertial drag force, respectively. The penetration depth and velocity of the projectile are denoted as z and v, respectively. The friction force is rate-independent of the penetrating projectile velocity. The local friction force between the particles and the projectile can be formulated based on the penetration model [30] as follows:

$$d\mathbf{F} = \alpha\mu_i(\rho g z)d\mathbf{A} \tag{2}$$

where $\mathbf{F}$, α, and μ_i denote the local friction force, experimental coefficient, and internal friction coefficient, respectively. The gravitational loading pressure is denoted by $\rho g z$, where ρ and g denote the particle density and gravitational acceleration, respectively. The total rate-independent friction force is determined by integrating over $d\mathbf{A}$, which is an infinitesimal area element that points normal to the projectile surface. Note that the friction between the granular particles and projectile acts normal to their surface of contact. Thus, the rate-independent friction force $f(z)$ can be determined by calculating the gravitational loading pressure exerted by granular particles in the direction perpendicular to the surface of the penetrating projectile. The friction force can be fitted to the power of the penetration depth based on the simulation and experimental data [31] using fitting parameters a and b as follows:

$$f(z) \simeq az^b \tag{3}$$

For the inertial drag force, the following governing equation was considered:

$$\sum F = ma = mg - f(z) - h(z)v^2 \tag{4}$$

where the projectile mass and acceleration are denoted as m and a, respectively. The kinetic energy of a projectile K is defined as follows:

$$K = \frac{1}{2}mv^2 \tag{5}$$

By differentiating the kinetic energy with respect to the penetration depth z and substituting it into Eq. (4), the governing equation is computed as follows:

$$\frac{dK}{dz} = mg - f(z) - \frac{2h(z)}{m}K \tag{6}$$

The solution to the above differential equation for the projectile can be obtained [32] as follows:

$$\begin{aligned} K(z) &= He^{-\int \frac{2h(z)}{m}dz} \\ H &= \int [mg - f(z)]\, e^{\int \frac{2h(z)}{m}dz}dz + K_0 \end{aligned} \tag{7}$$

where the kinetic energy when z=0 is denoted by K_0. With two different free-fall heights, the following equations can be formulated:

$$\begin{aligned} K_i(z) &= H_i e^{-\int \frac{2h(z)}{m}dz} \\ H_i &= \int [mg - f(z)]\, e^{\int \frac{2h(z)}{m}dz}dz + K_{i0} \\ K_j(z) &= H_j e^{-\int \frac{2h(z)}{m}dz} \\ H_j &= \int [mg - f(z)]\, e^{\int \frac{2h(z)}{m}dz}dz + K_{j0} \end{aligned} \tag{8}$$

where K_i and K_j are the kinetic energies of an identical projectile dropped at free-fall heights h_i and h_j ($h_i > h_j$),

respectively. The kinetic energies of the projectile when z= 0 are denoted by K_{i0} and K_{j0}. By obtaining two different kinetic energies with different impact velocities, the above equation can be further summarized as follows:

$$\frac{K_i(z) - K_j(z)}{K_{i0} - K_{j0}} = e^{-\int \frac{2h(z)}{m} dz} \tag{9}$$

The kinetic energies $K_i(z)$ and $K_j(z)$ were formulated, and their values became zero at the final penetration depths $z_{max,i}$ and $z_{max,j}$, respectively. Using a numerical approach, it was possible to obtain the projectile velocities with respect to the penetration depth. Piece-wise interpolations were employed, and the curves were resampled with equal penetration depths. Thus, the subtraction of the square velocities can be computed for the integration of $h(z)$ as follows:

$$\int_0^z h(z)dz = -\frac{m}{2} \ln \left[\frac{v_i^2(z) - v_j^2(z)}{v_{i0}^2 - v_{j0}^2} \right] \tag{10}$$

This equation can be simplified by finding the fitted curves based on experimental data [33] using fitting parameters c and d as follows:

$$\int_0^z h(z)dz \simeq cz^d \tag{11}$$

This fitted function is applicable to general cases, even for penetration depth values larger than $z_{\max,j}$ and $z_{\max,i}$. By substituting Eqs. (3) and (11) into the rate-independent friction and inertial drag forces in Eq. (7), nonlinear equations can be derived to determine the maximum penetration depth $z_{\max}$ as follows:

$$\int_0^{z_{\max}} \left(mg - az^b \right) e^{\frac{2cz^d}{m}} dz = -K_0 \tag{12}$$

Note that the equation for the maximum penetration depth has a solution in terms of an incomplete gamma function.

2.2 Discrete element method (DEM)

To analyze the cone-shaped projectile behavior during penetration into granular particles, large-scale simulations were performed using the discrete element method (DEM). The DEM simulation was performed using ABAQUS software. In the simulation, granular particles were set as discrete elements, and the projectile was modeled as a rigid body using the finite element method (FEM). The particle−projectile interactions were based on a hard contact model for rigid bodies. Particle−particle interactions were based on the contact force adopted by the Hertz–Mindlin model. A schematic of the contact model is shown in Fig. 2, where the model was composed of a spring, damper, and friction slider.

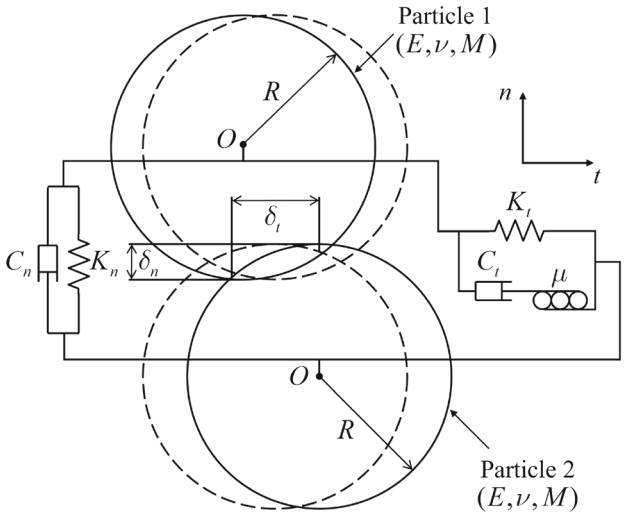

E : Young's Modulus of particle	K_t : Tangential elasticity constant
ν : Poisson's ratio of particle	K_n : Normal elasticity constant
M : Mass of particle	C_t : Tangential damping constant
R : Radius of particle	C_n : Normal damping constant
O : Particle center	δ_t : Tangential penetration depth
μ : Coulomb friction coefficient	δ_n : Normal penetration depth

Fig. 2 Schematic of the Hertz–Mindlin contact model

As the discrete numerical model for granular particles comprises forces in normal and tangential directions [34–37], the intergranular normal and tangential elastic forces based on the Hertzian and Mindlin–Deresiewicz models were considered in the contact processes. Nonlinear normal and tangential damping forces were also considered to account for energy dissipation during penetration. The contact forces were formulated as follows:

$$F_n = -F_n^e + F_n^d \tag{13}$$

$$F_t = \min \left\{ \mu F_n, F_t^e + F_t^d \right\} \tag{14}$$

$$F_n^e = K_n \delta_n = \frac{4}{3} E \sqrt{R\delta_n^3} \tag{15}$$

$$F_t^e = K_t \delta_t = 8G\delta_t \sqrt{R\delta_n} \tag{16}$$

$$F_n^d = -C_n v_n^{rel} = 2 \frac{v_n^{rel} \ln \varepsilon}{\sqrt{\ln^2 \varepsilon + \pi^2}} \sqrt{\frac{5}{6} M K_n} \tag{17}$$

$$F_t^d = -C_t v_t^{rel} = 2 \frac{v_t^{rel} \ln \varepsilon}{\sqrt{\ln^2 \varepsilon + \pi^2}} \sqrt{\frac{5}{6} M K_t} \tag{18}$$

where F^e and F^d denote elastic and damping forces, respectively. The subscripts n and t indicate normal and tangential components, respectively. The penetration depth during the overlap of particles, elasticity constant, damping constant, and relative velocity of the particles are denoted by δ, K, C, and v^{rel}, respectively. The restitution coefficient is denoted as

ε. The equivalent Young's modulus, shear modulus, radius, and mass are denoted as E, G, R, and M, respectively. Simulations were conducted to analyze the penetration behaviors of cone-shaped projectiles based on the particle interacting forces in the contact model.

3 Numerical methodology

3.1 Simulation setup

The initial properties of the granular particles and the parameters of the contact model were set as listed in Table 1. In the DEM simulation, the particles were initially modeled with a PD3D element with 6 mm diameter, 1200 kgm^{-3} density, 2500 MPa elastic modulus, 0.4 Poisson's ratio, and 0.9 restitution coefficient. The projectile was modeled as a rigid body having properties of steel with 7930 kgm^{-3} density. The friction coefficients of the Hertz–Mindlin and hard contact models were set to 0.25. A gravity load was applied to ensure free-fall of the projectile and static state of granular particles when no contact was made. The repose angle of the defined particle system was evaluated as 21.47° using the following formulation [16]:

$$\tan\theta_r = \frac{0.14}{z}\left(\frac{\rho_p}{\rho}\right)^{1/2} D_p^{2/3}(h_t)^{1/3} \tag{19}$$

where θ_r, z, ρ_p, D_p, and h_t are the repose angle, penetration depth, projectile density, projectile diameter, and total drop distance.

The positioning of granular particles and utilized projectiles is shown in Fig. 3. Projectiles with fixed lengths of 30 mm and tip half-angles of 25°, 30°, 35°, 40°, and 45° were compared to investigate the effect of the projectile tip angle on penetration behavior. Projectiles with fixed tip half-angles of 30° and lengths of 30, 40, and 50 mm were compared to investigate the effect of projectile length on penetration behavior. Cases involving particles with various diameters and densities were also conducted to investigate the penetration behavior under different particle properties. Projectile with length 30 mm and tip half-angle 30° was employed for these cases. For all DEM simulation cases, the base diameter of the projectile with the largest base area was 60 mm. As the wall effects on granular particle motions become negligible when the container diameter is five times larger than the projectile diameter [20], the particles were positioned in a rigid cylindrical container with 300 mm diameter and 150 mm length.

The overall simulation procedure is illustrated in Fig. 4. The DEM simulation was performed by setting the total simulation time and initial parameters, such as material properties, number of particles, projectile position, and initial

Table 1 Properties of granular particles

Particle initial material properties					
Element type	Diameter (mm)	Density (kgm^{-3})	Elastic Modulus (MPa)	Poisson's ratio	Restitution coefficient
PD3D	6.0	1200	2500	0.4	0.9
Particle interaction properties					
Particle–Particle		Particle–Projectile		Particle–Wall/Floor	
Contact model	Friction coefficient	Contact model	Friction coefficient	Contact model	Friction coefficient
Hertz–Mindlin	0.25	Hard contact	0.25	Hard contact	0.25

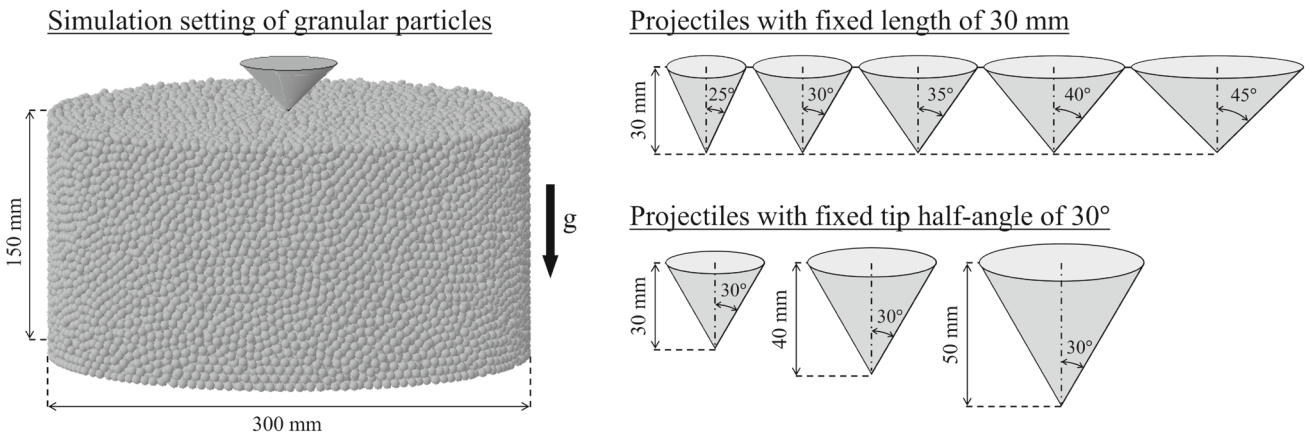

Fig. 3 Granular particle settings and cone-shaped projectiles with various parameters for DEM simulation

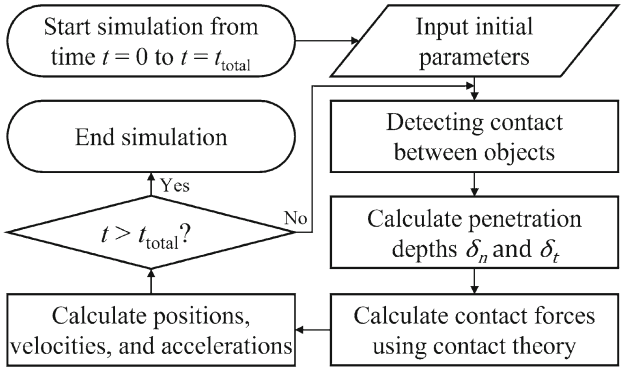

Fig. 4 DEM simulation procedure

projectile velocity. The time evolution data of the particle positions, velocities, accelerations, contact forces, and drag forces were obtained based on the initially defined contact models and material properties in the simulation. Penetration analyses were performed based on the setup to obtain friction force and inertial drag force data.

3.2 Penetration analysis

The rate-independent friction force refers to the gravitational loading pressure exerted by granular particles in the direction normal to the projectile surface. When a projectile penetrates granular particles at a constant velocity, a drag force consisting of the friction force and inertial drag force is exerted on the projectile. If the projectile velocity is lower than the critical velocity and results in a quasi-static condition, the inertial drag becomes negligible. This phenomenon occurs because the stabilization rate of the particles is faster than the scattering rate of the particles under quasi-static conditions. Thus the rate-independent friction force data can be obtained through simulation by setting the projectile to penetrate the granular particles at constant velocity lower than the critical velocity, and the overall process is shown in Fig. 5a. The critical velocity was formulated as follows [38]:

$$v_c = \sqrt{2gD} \tag{20}$$

where v_c and D are the critical velocity and particle diameter, respectively. By substituting the gravitational force value of 9.81 m/s^2 and particle diameter of 6 mm into Eq. (20), the critical velocity was calculated as approximately 343 mm/s. To ensure quasi-static conditions, the projectile velocity was set to 13 mm/s throughout the simulation to obtain the rate-independent friction force data. The data were analyzed to verify that the rate-independent friction force followed the power law with respect to the penetration depth.

The inertial drag force is related to the energy dissipation of the projectile to particles in contact. The process of obtaining inertial drag force data through DEM simulation requires more steps than those required for obtaining friction force data. Referring to Eqs. (9) and (10), the inertial drag force coefficient can be determined by obtaining the veloc-

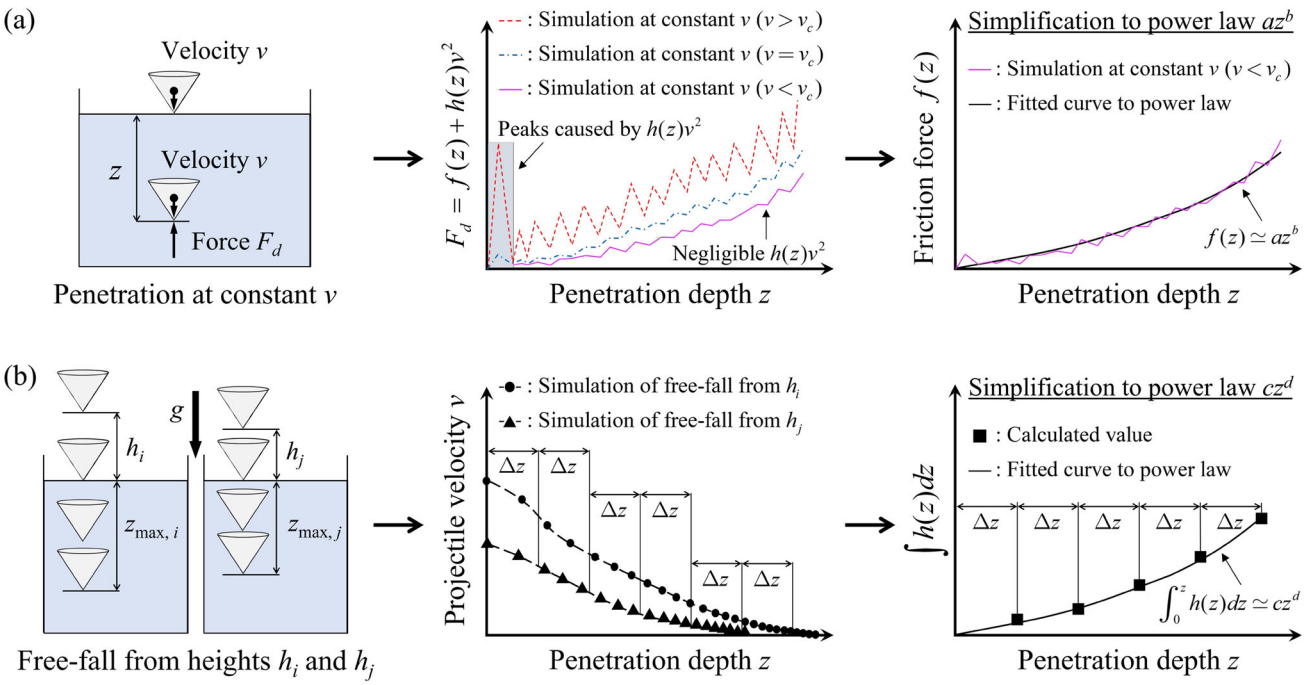

Fig. 5 Calculation of forces related to penetration into granular particles using DEM simulation. **a** Calculation of friction force $f(z)$ by implementing quasi-static condition, and **b** calculation of $\int h(z)dz$ related to the inertial drag force by implementing dynamic collision

ities of the free-falling projectiles at two different heights. The subtraction of the square velocities can be computed for integration of the inertial drag force coefficient. Thus, projectiles were set to free-fall onto granular particles to obtain data, and the overall process is shown in Fig. 5b. The free-fall heights h_i and h_j were set to 500 and 300 mm, respectively, throughout the simulation. The data were analyzed to verify that the integral values followed the power law with respect to the penetration depth.

4 Results and discussion

4.1 Rate-independent friction force

The quasi-static penetration process of the projectile is shown in Fig. 6. In the figure, the penetration depth and projectile length are expressed as z and L_p, respectively. The cases $z < L_p$, $z = L_p$, and $z > L_p$ indicate partial penetration, full penetration, and post-penetration processes, respectively. The projectile velocity was kept constant at 13 mm/s throughout the penetration process. Owing to the quasi-static nature of the penetration process, the particles did not disperse after coming in contact with the penetrating projectile. Based on the particle velocities, it could be observed that the volume of the displaced particles changed depending on the penetration process. The range of displaced particles interacting with the bottom area expanded in volume during partial penetration, resulting in the volume of displaced particles to be proportional to the third power of the penetration depth. After complete penetration, the range of displaced particles only increased vertically above the projectile, while the number of particles interacting with the bottom area remained constant. This induced the volume of the displaced particles to increase proportionally to the penetration depth throughout the post-penetration process.

The simulation data of the changes in rate-independent friction force with respect to the penetration depth are shown in Fig. 7. The first two sub-figures in the respective figure show the results obtained with different projectiles, while the latter two sub-figures present the results using varying particles. The results of curve fitting of the simulation data for the friction force are presented in Tables 2 and 3. Figure 7a shows the friction force exerted on projectiles with different tip angles. The projectile length was kept constant at 30 mm. Regions I and II specify partial penetration and post-penetration steps, respectively. It is noteworthy that the tendency of the friction force changed when the penetration depth became 30 mm. The force is proportional to the third power of the penetration depth and is linearly proportional to the penetration depth during the partial penetration and post-penetration processes. Moreover, projectiles with larger tip angles experience a greater friction force, where the force is proportional to the tangent square of the projectile tip angle throughout projectile penetration.

Figure 7b shows the friction force exerted on projectiles with different projectile lengths. The half-angles of the projectile tip were constant at 30°. The boundary that divides regions I and II is different for each projectile owing to their different projectile lengths. The relationship between the friction force and penetration depth can also be observed from this graph. It can also be observed that the friction force during partial penetration is identical for all three projectiles. The friction force varied only after each projectile had fully penetrated the granular particles. This indicates that the projectile length affects only the friction force after complete penetration of the projectiles. Based on the results shown in Figs. 7a, b, and Table 2, the rate-independent friction force can be fitted to the power of penetration depth as follows:

$$f_p(z) = a_1 z^3 \tan^2\theta \tag{21}$$

$$f_f(z) = a_2 z L_p^2 \tan^2\theta + (a_1 - a_2) L_p^3 \tan^2\theta \tag{22}$$

where $f_p(z)$ and $f_f(z)$ denote the friction force during partial penetration ($z \leq L_p$) and after full penetration ($z > L_p$), respectively. The half-angle of the tip is denoted by θ. The constants a_1 and a_2 were calculated as $(1.419 \pm 0.144) \cdot 10^{-4}$ Nmm^{-3} and $(1.634 \pm 0.246) \cdot 10^{-4}$ Nmm^{-3}, respectively. It is worth noting that the changing relationship between friction force and penetration depth before and after complete penetration corresponds to the changing trend of the relationship between displaced particle volume and penetra-

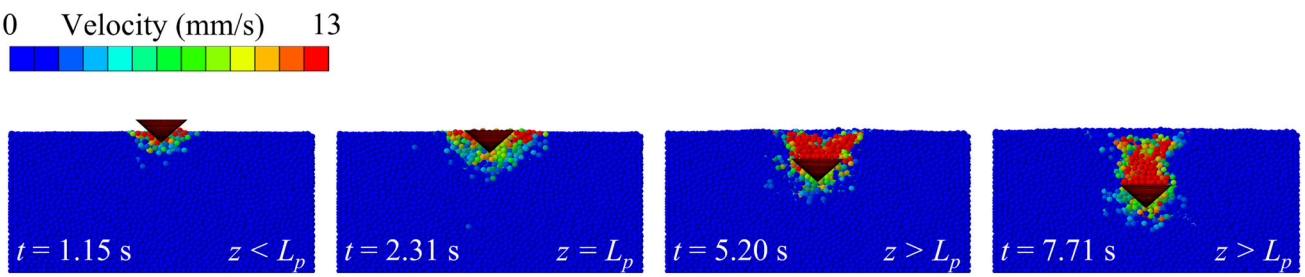

Fig. 6 DEM simulation process of projectile penetration at quasi-static condition (θ=45°, L_p=30 mm, D=6 mm, ρ=1200 kgm^{-3})

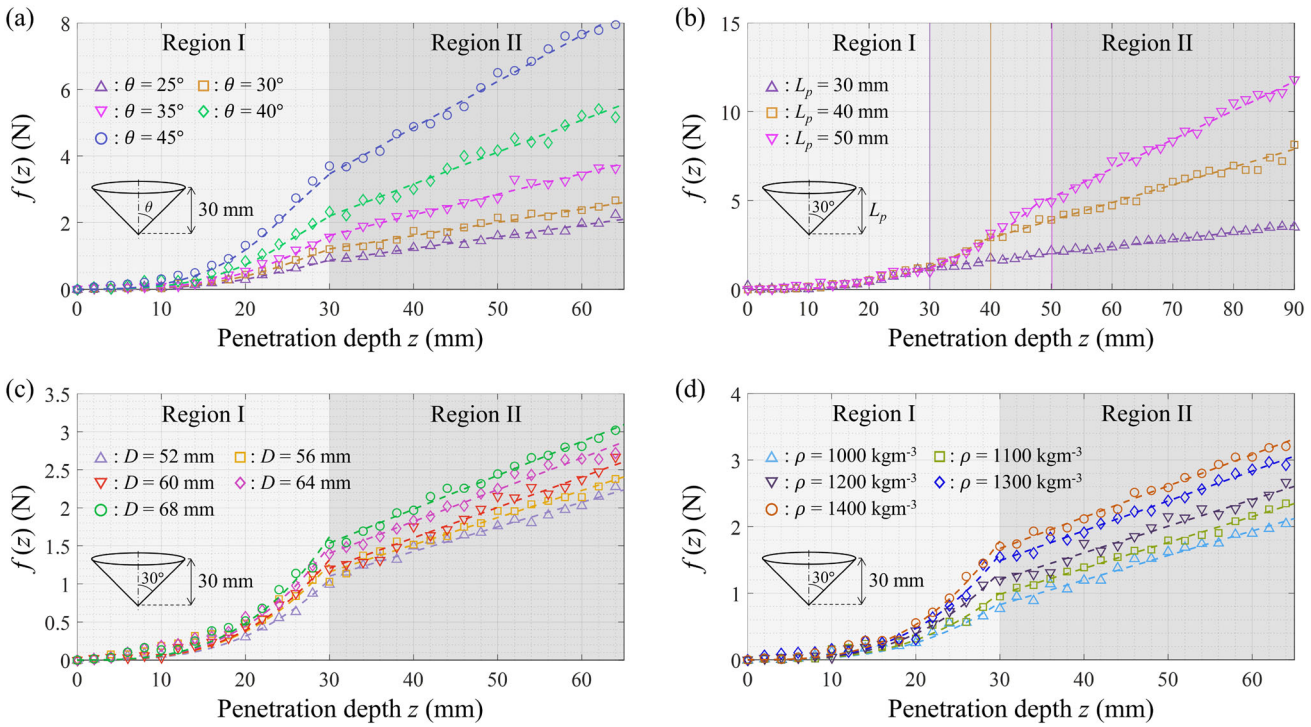

Fig. 7 Calculation of $f(z)$ at low projectile velocity (v=13 mm/s). **a** Projectiles with different tip angles θ, **b** projectiles with different lengths L_p, **c** particles with different diameters D, and **d** particles with different densities ρ

Table 2 Fitted $f(z)$ for varying projectile parameters

Projectile parameters		Fitted curves of $f(z)$	
θ (°)	L_p (mm)	Region I	Region II
25	30	$3.699\times10^{-5}z^3$	$0.0352z-0.190$
30	30	$4.882\times10^{-5}z^3$	$0.0399z+0.009$
35	30	$6.251\times10^{-5}z^3$	$0.0613z-0.229$
40	30	$9.157\times10^{-5}z^3$	$0.0968z-0.712$
45	30	$1.442\times10^{-4}z^3$	$0.1400z-0.761$
30	40	$4.708\times10^{-5}z^3$	$0.1001z-1.128$
30	50	$4.459\times10^{-5}z^3$	$0.1635z-3.021$

Table 3 Fitted $f(z)$ for varying particle parameters

Particle parameters		Fitted curves for $f(z)$	
D (mm)	ρ (kgm^{-3})	Region I	Region II
5.2	1200	$3.914\times10^{-5}z^3$	$0.0324z+0.132$
5.6	1200	$4.663\times10^{-5}z^3$	$0.0356z+0.089$
6.0	1200	$4.882\times10^{-5}z^3$	$0.0399z+0.009$
6.4	1200	$5.569\times10^{-5}z^3$	$0.0418z+0.148$
6.8	1200	$5.998\times10^{-5}z^3$	$0.0444z+0.204$
6.0	1000	$3.189\times10^{-5}z^3$	$0.0369z-0.280$
6.0	1100	$3.715\times10^{-5}z^3$	$0.0389z-0.181$
6.0	1300	$5.871\times10^{-5}z^3$	$0.0448z+0.144$
6.0	1400	$6.607\times10^{-5}z^3$	$0.0470z+0.260$

tion depth discussed in the previous section. This analysis is in good agreement with the modified Archimedes' law proposed in [40] which states resistance force in quasi-static condition is linearly proportional to the volume of the displaced granular materials.

To confirm the suitability of the formulations to general cases of cone-shaped projectile penetration, cases were conducted involving various particle properties. These cases utilized a projectile with length 30 mm and tip half-angle 30°. Figure 7c shows the friction force exerted by particles with different diameters while keeping the particle density constant at 1200 kgm^{-3}. Figure 7d presents the friction force exerted by particles with varying densities, with the diameter fixed at 6.0 mm. In both cases, the relationship between friction force and penetration depth follows the proposed formulations, where the force is proportional to the third power of the penetration depth and maintains a linear proportionality during the partial penetration and post-penetration processes. The constants a_1 and a_2 exhibit a linear relationship with both particle diameter and density. Based on the results shown in Table 3, it can be evaluated that a_1 and a_2 increase by $3.907{\cdot}10^{-5}$ Nmm^{-3} and $2.500{\cdot}10^{-5}$ Nmm^{-3}, respectively, for every 1 mm increase in particle diameter. Additionally, the constants increase by $2.564{\cdot}10^{-7}$ Nmm^{-3} and $8.417{\cdot}10^{-8}$ Nmm^{-3}, respectively, for every 1 kgm^{-3} increase in particle density.

4.2 Physics behind the variation of friction force with changing contact area

The rate-independent friction force refers to the gravitational loading pressure exerted by granular particles in the direction normal to the projectile surface. Thus, the changing tendency of the friction force with respect to the penetration depth before and after full penetration can be explained by the changes in the contact area between the penetrating projectile and granular particles. An illustration of the contact area between the projectile and particles before and after full penetration is shown in Fig. 8. The contact area during partial penetration A_p can be formulated as follows:

$$A_p = \pi(z\tan\theta)\left(\frac{z}{\cos\theta}\right) \propto \left(\frac{\tan\theta}{\cos\theta}\right) z^2 \tag{23}$$

The pressure in the y-direction was considered considering the projectile's penetration direction. Pressure p_y can be formulated as follows:

$$p_y = \alpha\mu\rho g z\sin\theta \propto z\sin\theta \tag{24}$$

The rate-independent friction force was determined by multiplying the particle contact area and the pressure in the y-direction. Thus, the frictional force during partial penetration $f_p(z)$ can be formulated as follows:

$$f_p(z) \propto z^3\tan^2\theta \tag{25}$$

For cases after full penetration, the contact area A_f can be formulated as follows:

$$A_f = \pi(L_p\tan\theta)\left(\frac{L_p}{\cos\theta}\right) \propto \left(\frac{\tan\theta}{\cos\theta}\right) L_p^2 \tag{26}$$

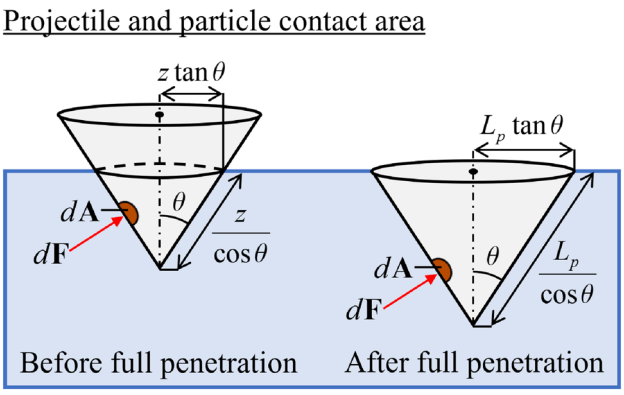

Fig. 8 Illustration of changing projectile contact area as a result of coming in contact with granular particles during partial penetration and after full penetration

Because of the change in the contact area formulation, the friction force after full penetration $f_f(z)$ is formulated as follows:

$$f_f(z) \propto zL_p^2\tan^2\theta \tag{27}$$

Note that the pressure formulation was constant for all the projectile penetration cases. Therefore, the rate-independent friction force follows the changing power law with respect to penetration depth, as presented in the previous section.

4.3 Inertial drag force

The dynamic penetration process is shown in Fig. 9. The projectile was set to free-fall onto granular particles from heights of 500 and 300 mm. Owing to the dynamic nature of the penetration process, the particles dispersed after coming in contact with the penetrating projectile. Therefore, the projectile was visible from the top view, even after full penetration into the granular particles. Based on the particle velocities, it can be observed that the range of particles interacting with the projectile changed depending on the penetration process. Although the range of particle interactions increased with increasing penetration depth during partial penetration, it remained constant after complete penetration. The dynamic collision of the projectile resulted in the dispersion of particles, thereby preventing the stacking of particles onto the penetrating projectile. Moreover, the cavity diameter D_c remained unchanged during the post-penetration step. This indicates that no interactions occurred on the top area of the projectile, while the number of particles interacting with the bottom area was kept constant. Thus, the total number of particle interactions with the projectile remained constant throughout the post-penetration process.

The integral of the inertial drag force coefficient was obtained based on a dynamic penetration simulation. The simulation data for the changes in the integral value with respect to the penetration depth and their fitted curves are shown in Fig. 10. The initial two sub-figures in the given figure show the results obtained with different projectiles, while the subsequent two sub-figures present the results obtained using varying particles. The results of the curve fitting of the simulation data for the integral of the inertial drag force coefficient are presented in Tables 4 and 5. Figure 10a shows the results when projectiles with different tip angles were simulated. The projectile length was kept constant at 30 mm. Regions I and II indicate partial penetration and post-penetration processes, respectively. Similar to the friction force, the integral values showed changing tendencies before and after complete penetration. The integral of the inertial drag force coefficient was proportional to the second and first powers of the penetration depth during the partial penetration and post-penetration processes, respec-

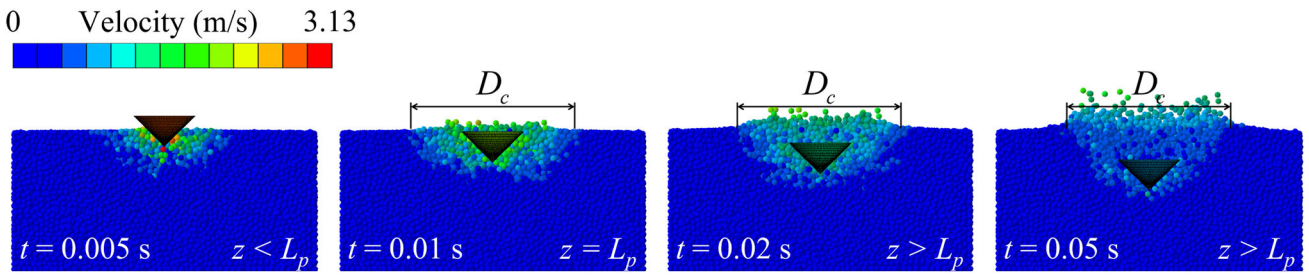

Fig. 9 DEM simulation process of projectile free-fall from a height of 0.5 m (θ=45°, L_p=30 mm, D=6 mm, ρ=1200 kgm^{-3})

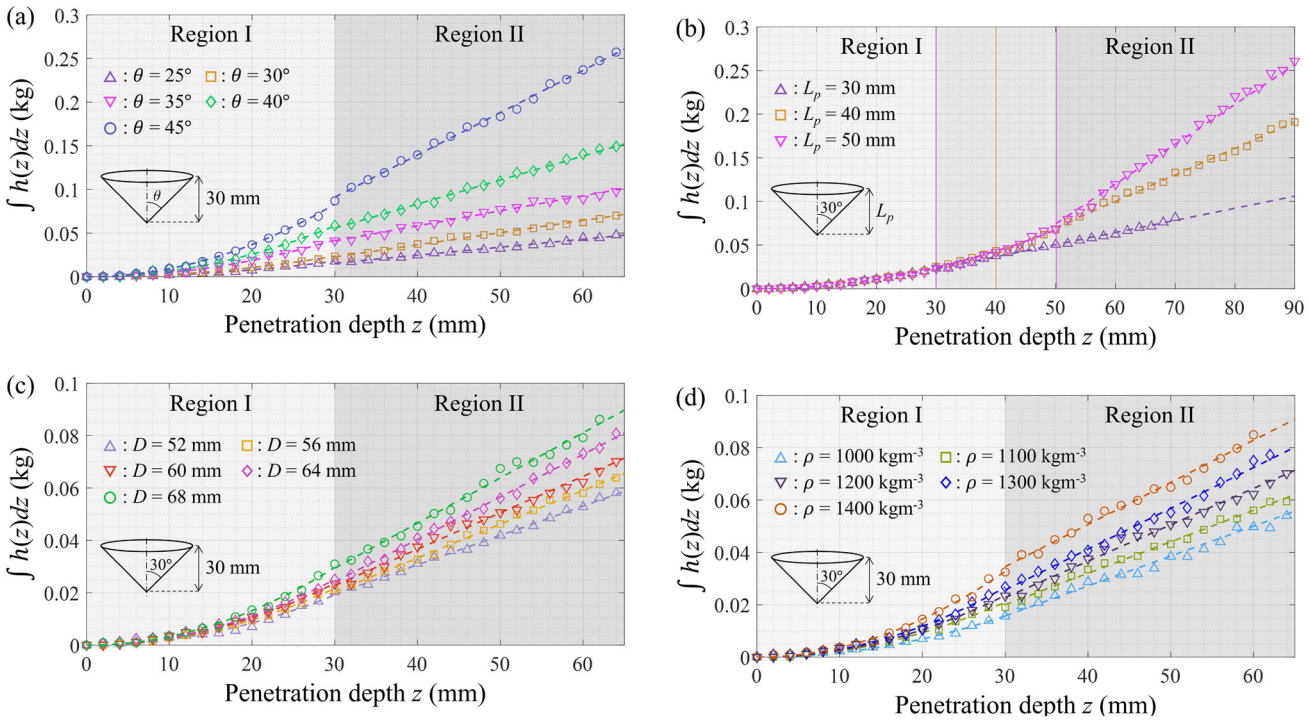

Fig. 10 Calculation of $\int h(z)dz$ using free-fall of projectile. (a) Projectiles with different tip angles θ, (b) projectiles with different lengths L_p, (c) particles with different diameters D, and (d) particles with different densities ρ

Table 4 Fitted $\int h(z)dz$ for varying projectile parameters

Projectile parameters		Fitted curves of $\int h(z)dz$	
θ (°)	L_p (mm)	Region I	Region II
25	30	$1.978\times10^{-5}z^2$	$0.00092z-0.0120$
30	30	$2.622\times10^{-5}z^2$	$0.00139z-0.0189$
35	30	$4.682\times10^{-5}z^2$	$0.00172z-0.0105$
40	30	$6.464\times10^{-5}z^2$	$0.00275z-0.0269$
45	30	$9.235\times10^{-5}z^2$	$0.00485z-0.0543$
30	40	$2.729\times10^{-5}z^2$	$0.00303z-0.0819$
30	50	$2.688\times10^{-5}z^2$	$0.00456z-0.1538$

Table 5 Fitted $\int h(z)dz$ for varying particle parameters

Particle parameters		Fitted curves for $\int h(z)dz$	
D (mm)	ρ (kgm^{-3})	Region I	Region II
5.2	1200	$2.127\times10^{-5}z^2$	$0.00112z-0.0142$
5.6	1200	$2.407\times10^{-5}z^2$	$0.00129z-0.0183$
6.0	1200	$2.622\times10^{-5}z^2$	$0.00139z-0.0189$
6.4	1200	$2.789\times10^{-5}z^2$	$0.00162z-0.0245$
6.8	1200	$3.295\times10^{-5}z^2$	$0.00172z-0.0223$
6.0	1000	$1.743\times10^{-5}z^2$	$0.00114z-0.0184$
6.0	1100	$2.337\times10^{-5}z^2$	$0.00120z-0.0160$
6.0	1300	$2.963\times10^{-5}z^2$	$0.00156z-0.0211$
6.0	1400	$3.639\times10^{-5}z^2$	$0.00161z-0.0137$

tively. Moreover, the value was proportional to the tangent square of the tip angle throughout the penetration process.

Figure 10b shows the results when projectiles with different projectile lengths were simulated. The projectiles had a constant tip half-angle of 30°. In addition to the changing relationship between the integral value and penetration depth,

we observed that all projectiles had identical integral values during the process of partial penetration. The values differed only after complete penetration of the projectiles. This indicates that the projectile length affects only the integral value during the post-penetration step. Based on the results shown in Figs. 10a, b, and Table 4, the integral of the inertial drag force coefficient can be fitted to the penetration depth power as follows:

$$\int h_p(z)dz = c_1 z^2 \tan^2\theta \tag{28}$$

$$\int h_f(z)dz = c_2 z L_p^2 \tan^2\theta + (c_1 - c_2 L_p) L_p^2 \tan^2\theta \tag{29}$$

where $\int h_p(z)dz$ and $\int h_f(z)dz$ denote the integral of the inertial drag force coefficient during partial penetration ($z \leq L_p$) and after full penetration ($z > L_p$), respectively. The constants c_1 and c_2 were calculated as $(8.740 \pm 0.677) \cdot 10^{-5}$ kgmm^{-2} and $(4.874 \pm 0.658) \cdot 10^{-6}$ kgmm^{-3}, respectively.

Cases involving various particle properties were conducted using a projectile with length 30 mm and tip half-angle 30° to consider randomness of particle materials. Figure 10c and d shows the results with different particle diameters and densities, respectively. It can be observed from both cases that the relationship between integral value and penetration depth follows the proposed formulations. The constants c_1 and c_2 demonstrate a linear correlation with both particle diameter and density. Based on the results presented in Table 5, it can be evaluated that c_1 and c_2 increase by $2.190 \cdot 10^{-5}$ kgmm^{-2} and $1.250 \cdot 10^{-6}$ kgmm^{-3}, respectively, for 1 mm increase in particle diameter. The constants increase by $1.422 \cdot 10^{-7}$ kgmm^{-2} and $3.917 \cdot 10^{-9}$ kgmm^{-3}, respectively, for every 1 kgm^{-3} increase in particle density.

Based on the simplified equation, the inertial drag force coefficient function can be formulated with respect to the penetration depth as follows:

$$h_p(z) = 2c_1 z \tan^2\theta \tag{30}$$

$$h_f(z) = c_2 L_p^2 \tan^2\theta \tag{31}$$

where $h_p(z)$ and $h_f(z)$ denote the inertial drag force coefficient during partial penetration and after full penetration, respectively. It can be seen that the coefficient is proportional to the penetration depth during partial penetration, but becomes independent of the penetration depth after full penetration into the particles.

4.4 Physics behind the variation of drag force with fluidization

The inertial drag force is related to the energy dissipation of the projectile to the particles in contact. The changing tendency of the inertial drag force coefficient with respect to the penetration depth before and after full penetration can be explained by the fluidization of granular particles. Impact of an object with a velocity higher than the critical velocity v_c causes a granular bed to be fluidized and behave like liquid during the impact [39, 40]. Thus, the inertial drag force for granular particles and fluids can be expressed as follows:

$$h(z)v^2 = \frac{1}{2} C_d(z) \mu_f A v^2 \tag{32}$$

where $C_d(z)$ and μ_f denote the fluid drag coefficient and density, respectively. The cross-sectional area of the projectile during immersion is denoted as A. Thus, the inertial drag coefficient during partial penetration $h_p(z)$ can be formulated as follows:

$$h_p(z) = \frac{1}{2} C_d(z) \mu_f \pi z^2 \tan^2\theta \tag{33}$$

The fluid drag coefficient can be formulated as a function of penetration depth, and experimental studies have been conducted to verify that the coefficient is proportional to the inverse of the penetration depth during the early stages of penetration [41]. Therefore, the inertial drag coefficient during partial penetration can be formulated using the penetration depth and projectile tip angle as follows:

$$h_p(z) \propto z \tan^2\theta \tag{34}$$

Using Eq. (32), the inertial drag coefficient after full penetration $h_f(z)$ can be formulated as follows:

$$h_f(z) = \frac{1}{2} C_d(z) \mu_f \pi L_p^2 \tan^2\theta \tag{35}$$

After full penetration, the fluid drag coefficient becomes constant and independent of the penetration depth. Thus, the inertial drag coefficient after full penetration can be formulated using the projectile length and tip angle as follows:

$$h_f(z) \propto L_p^2 \tan^2\theta \tag{36}$$

Therefore, the inertial drag force coefficient follows the changing power law with respect to penetration depth, as presented in the previous section. The drag force coefficient is linearly proportional to the penetration depth during partial penetration, and it is independent of the penetration depth after full penetration.

5 Experimental verification

Experiments were conducted to validate that the friction and inertial drag forces follow the power law with respect to

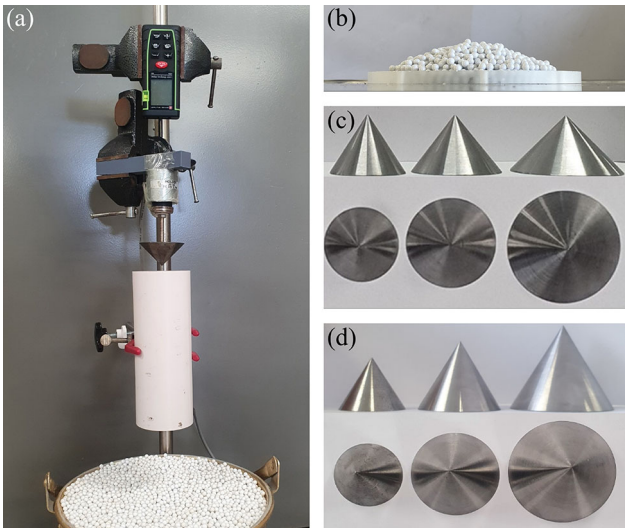

Fig. 11 **a** Experimental setup for verification of simplified force terms, **b** piled beads to measure repose angle, **c** utilized projectiles with equal lengths, and **d** utilized projectiles with equal tip angles

penetration depth. Projectiles were dropped onto granular particles to obtain penetration depth values. The changing penetration depth over the penetration time period and maximum penetration depth values were compared with the numerically calculated values.

5.1 Experiment setup

The experimental setup is shown in Fig. 11a. ABS plastic beads with a diameter of 6 mm were used as the granular particles in the experiment. A cone-shaped steel projectile was fixed and dropped using an electromagnetic holder. A cylinder guide was utilized to minimize the horizontal movement of the projectile during free-fall onto the particles. The repose angle of the plastic beads was measured to ensure that they adequately represent the particle systems used in the DEM simulations. The piled beads are shown in Fig. 11b, and the repose angle was measured to be approximately 22°. This value closely aligns with the evaluated repose angle of 21.47° for the particle system used in the DEM simulation.

As the projectile became undetectable after full penetration, a bolt was connected to the top of the projectile and a high-speed camera tracked the end of the bolt to acquire time-varying penetration depth data. A laser distance meter was used to obtain maximum penetration depth data. Projectiles with various lengths and tip angles shown in Figs. 11c and d were dropped to ensure that the power law model applied to all penetration cases. At least 20 trials were conducted for each projectile to obtain accurate and consistent experimental results.

5.2 Comparison of time-varying penetration depth

A projectile with a tip half-angle of 45° and length of 30 mm was used in the experiment. The projectile was dropped from a height of 0.1 m using an electromagnetic holder and captured by a high-speed camera. In the data processing procedure, the projectile positions at each frame were tracked using the tracker program to mark the projectile positions in the reference x–y coordinate system, as shown in Fig. 12. The processed projectile position data allowed the analysis of the penetration depth over the penetration period.

For comparison with the experimental results, the penetration depth was numerically processed using the simplified terms of the friction and inertial drag forces. Equation (7) is used to formulate the projectile velocity in terms of the projectile kinetic energy and mass as follows:

$$v(z) = \sqrt{\frac{2K(z)}{m}} \tag{37}$$

The projectile kinetic energy is expressed using the simplified terms of the friction and inertial drag forces. The penetration depth over the penetration period was determined using the calculated projectile velocity. The experimental and numerical results are presented in Fig. 13. Although the final penetration depth differs slightly by an approximate value of 1.8 mm, the tendencies of the depth values show great agreement between the experimental and numerical results throughout the overall penetration process. This indicates that the rate-independent friction force and inertial drag force were accurately simplified to terms related to the penetration depth values.

5.3 Comparison of maximum penetration depth

To further verify the accuracy of the simplified force terms, the experiment was expanded to determine the maximum penetration depths of the various projectiles. Two sets of experiments were conducted: the first set investigated projectiles with varying tip angles, and the second set investigated projectiles with varying lengths. In the first set, projectiles with fixed lengths of 30 mm and base diameters of 25, 30, 35, 40, 48, and 60 mm were investigated. In the second set, projectiles with fixed tip half-angles of 30° and lengths of 30, 40, and 50 mm were investigated. The projectiles were dropped from a constant height of 0.1 m using the electromagnetic holder. The final penetration depths were obtained by measuring the distance to the top of the projectile using a laser distance meter.

For comparison with the experimental results, the maximum penetration depths were numerically processed using Eq. (12), which uses the simplified terms of the friction and inertial drag forces. The experimental and numerical

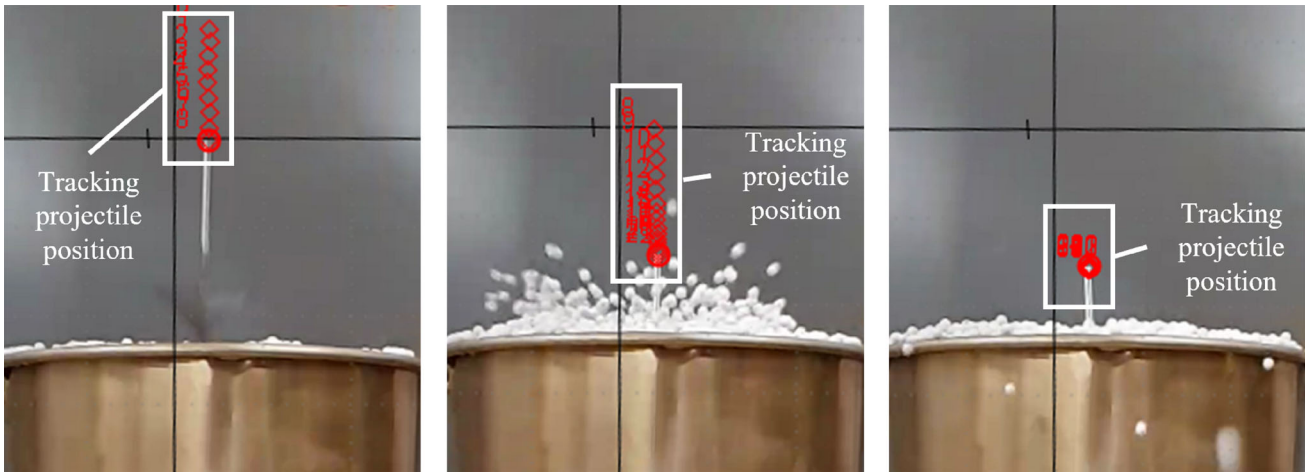

Fig. 12 Tracking of projectile position at each frame using tracker program (https://physlets.org/tracker/)

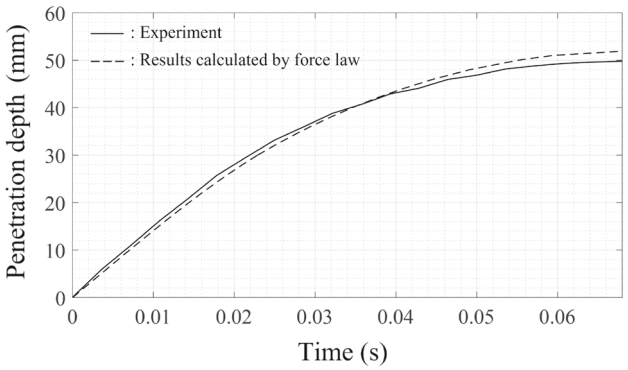

Fig. 13 Example of depth versus time of a projectile ($\theta = 45°$, L_p=30 mm) dropped from a height of 0.1 m

results are shown in Fig. 14. Figure 14a shows the results for the projectiles with different tip angles. The experimental and numerical results show similar tendencies, where a projectile with a half-angle of 33.7° results in the greatest maximum penetration depth for both the experimental and numerical results. The difference between the experimental and numerical values is the largest for a projectile with a half-angle of 45°, where the difference is approximately 1.9 mm. Considering that the projectile is dropped at a height of 0.1 m, the difference in penetration depth of 1.9 mm is relatively small and negligible. Thus, it can be observed from the results that the experimental and numerical results are in good agreement for projectiles with various tip angles. Figure 14b shows the results for projectiles of different lengths. Both the experimental and numerical results showed that projectiles with greater lengths resulted in greater maximum penetration depth values. The difference between the experimental and numerical values was the largest for projectiles with a length of 50 mm, where the difference was approximately 2.7 mm. Again, the difference is relatively small compared to that with the dropped height of 0.1 m. Thus, the result shows that experimental and numerical results show agreement for projectiles

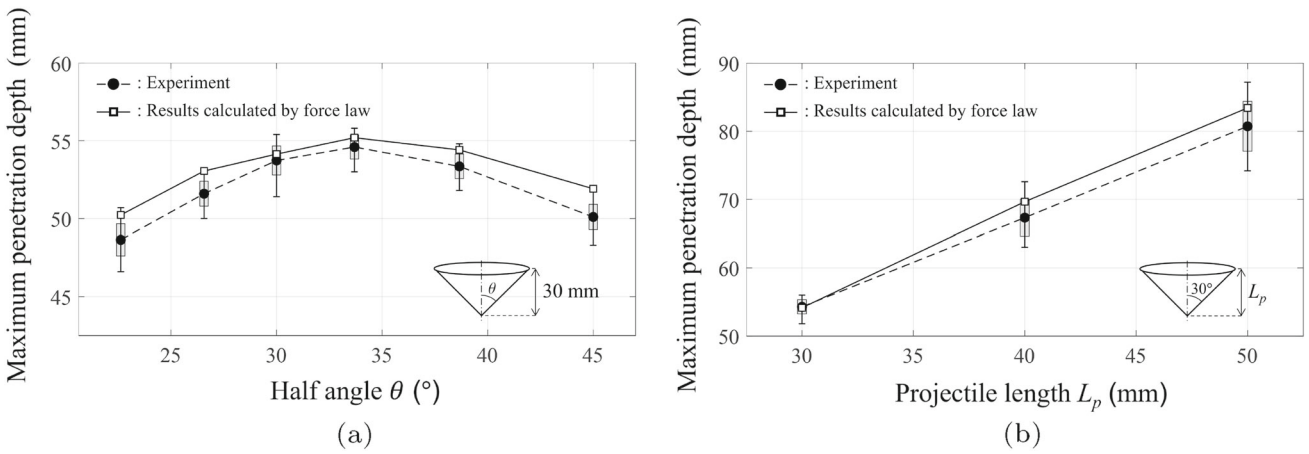

Fig. 14 Experimental verification of simplified force terms using maximum penetration depth. **a** Projectiles with different tip angles θ, and **b** projectiles with different lengths L_p

with varying lengths. The experimental results showed that the simplified force law applies accurately to projectiles with various tip angles and lengths, where the maximum penetration depths can be accurately predicted using numerical methods.

6 Conclusions

In this study, cone-shaped projectile behavior during penetration of granular particles was analyzed using simulations based on the discrete element method (DEM). The interaction force between the projectile and particles comprises a rate-independent friction force and inertial drag force proportional to the squared projectile velocity. Simulations show that the friction and inertial drag forces result in changing behaviors before and after full penetration of the particles. The friction force was proportional to the third power of the penetration depth and linearly proportional to the penetration depth during the partial penetration and post-penetration processes, respectively. The inertial drag force was linearly proportional and independent of the penetration depth during the partial penetration and post-penetration processes. Based on the simulated results, the force terms were simplified to the power of the penetration depth, where the projectile tip angle and length were coefficients. The simplified terms are physically explained using changes in the contact area and fluidization of particles during dynamic collisions. To verify the accuracy of the simplified terms, experiments were conducted to compare the experimental results with the numerical results processed using simplified terms. The experiments were conducted by dropping cone-shaped steel projectiles onto ABS plastic beads to acquire projectile position and penetration depth data using a high-speed camera and laser distance meter. The experimental and numerical results show good agreement in terms of the penetration depth change over the penetration time period and final penetration depth values. Thus, the experiment successfully shows that the simplified force law applies accurately to the penetration behavior of cone-shaped projectiles. In conclusion, this study proposes and validates mathematical models of the rate-independent friction force and inertial drag force to explain the behavior of cone-shaped projectiles during penetration into granular particles.

Acknowledgements This study was supported by the National Research Foundation of Korea (NRF) grant funded by the Korean government (MSIT) (No.2018R1A5A7025522).

Declarations

Conflict of interest The authors declare that they have no known competing financial interests or personal relationships that could have appeared to influence the work reported in this paper.

References

1. Horabik J, Molenda M (2016) Parameters and contact models for DEM simulations of agricultural granular materials: A review. Biosys Eng 147:206–225. https://doi.org/10.1016/j.biosystemseng.2016.02.017
2. Lim NH, Kim KJ, Bae HU, Kim S (2020) DEM analysis of track ballast for track ballast-wheel interaction simulation. Appl Sci 10(8):2717. https://doi.org/10.3390/app10082717
3. Zhou L, Gao J, Cheng P, Hu C (2020) Study on track-soil traction using discrete element method simulation and soil bin test. AIP Adv 10(7):075307. https://doi.org/10.1063/5.0016448
4. Mudarisov S, Farkhutdinov I, Khamaletdinov R, Khasanov E, Mukhametdinov A (2022) Evaluation of the significance of the contact model particle parameters in the modelling of wet soils by the discrete element method. Soil and Tillage Res 215:105228. https://doi.org/10.1016/j.still.2021.105228
5. Nordstrom KN, Lim E, Harrington M, Losert W (2014) Granular dynamics during impact. Phys Rev Lett 112(22):228002. https://doi.org/10.1103/PhysRevLett.112.228002
6. Xu Y, Padding JT, Kuipers JAM (2014) Numerical investigation of the vertical plunging force of a spherical intruder into a prefluidized granular bed. Phys Rev E 90(6):062203. https://doi.org/10.1103/PhysRevE.90.062203
7. Zaidi AA, Müller C (2017) Vertical drag force acting on intruders of different shapes in granular media. In: EPJ Web of Conferences. Vol.140. EDP Sciences. pp 02011. doi:https://doi.org/10.1051/epjconf/201714002011
8. Roth LK (2021) Constant speed penetration into granular materials: drag forces from the quasistatic to inertial regime. Granular Matter 23(3):1–17. https://doi.org/10.1007/s10035-021-01106-5
9. Feng Y, Blumenfeld R, Liu C (2019) Support of modified Archimedes' law theory in granular media. Soft Matter 15(14):3008–3017. https://doi.org/10.1039/C8SM02480D
10. Cheng B, Yu Y, Baoyin H (2018) Collision-based understanding of the force law in granular impact dynamics. Phys Rev E 98(1):012901. https://doi.org/10.1103/PhysRevE.98.012901
11. Hou M, Peng Z, Liu R, Lu K, Chan CK (2005) Dynamics of a projectile penetrating in granular systems. Phys Rev E 72(6):062301. https://doi.org/10.1103/PhysRevE.72.062301
12. Ogawa K, Takeda S, Kobayashi H (2015) Dynamic simulations of projectile penetration into granular medium. Mech Eng J 2(1):14–00427. https://doi.org/10.1299/mej.14-00427
13. Zaidi AA (2018) Study of particle inertia effects on drag force of finite sized particles in settling process. Chem Eng Res Des 132:714–728. https://doi.org/10.1016/j.cherd.2018.02.013
14. Chian SC, Tan BCV, Sarma A (2017) Reprint of: Projectile penetration into sand: Relative density of sand and projectile nose shape and mass. Int J Impact Eng 105:80–88. https://doi.org/10.1016/j.ijimpeng.2017.03.026
15. Cheng B, Yu Y, Baoyin H (2017) Asteroid surface impact sampling: dependence of the cavity morphology and collected mass on projectile shape. Sci Rep 7(1):1–10. https://doi.org/10.1038/s41598-017-10681-8
16. Newhall KA, Durian DJ (2003) Projectile-shape dependence of impact craters in loose granular media. Phys Rev E 68(6):060301. https://doi.org/10.1103/PhysRevE.68.060301
17. Zaidi AA (2020) Granular drag force during immersion in dry quicksand. Powder Technol 364:986–993. https://doi.org/10.1016/j.powtec.2019.10.048
18. Nouguier-Lehon C, Vincens E, Cambou B (2005) Structural changes in granular materials: the case of irregular polygonal particles. Int J Solids Struct 42(24–25):6356–6375. https://doi.org/10.1016/j.ijsolstr.2005.04.021

19. Uehara JS, Ambroso MA, Ojha RP, Durian DJ (2003) Low-speed impact craters in loose granular media. Phys Rev Lett 90(19):194301. https://doi.org/10.1103/PhysRevLett.90.194301
20. Seguin A, Bertho Y, Gondret P (2008) Influence of confinement on granular penetration by impact. Phys Rev E 78(1):010301. https://doi.org/10.1103/PhysRevE.78.010301
21. Goldman DI, Umbanhowar P (2008) Scaling and dynamics of sphere and disk impact into granular media. Phys Rev E 77(2):021308. https://doi.org/10.1103/PhysRevE.77.021308
22. Hou M, Peng Z, Liu R, Lu K, Chan CK (2005) Dynamics of a projectile penetrating in granular systems. Phys Rev E 72(6):062301. https://doi.org/10.1103/PhysRevE.72.062301
23. Ambroso MA, Kamien RD, Durian DJ (2005) Dynamics of shallow impact cratering. Phys Rev E 72(4):041305. https://doi.org/10.1103/PhysRevE.72.041305
24. Katsuragi H, Durian DJ (2013) Drag force scaling for penetration into granular media. Phys Rev E 87(5):052208. https://doi.org/10.1103/PhysRevE.87.052208
25. Katsuragi H, Durian DJ (2007) Unified force law for granular impact cratering. Nat Phys 3(6):420–423. https://doi.org/10.1038/nphys583
26. Shen W, Zhao T, Crosta GB, Dai F, Dattola G (2022) Influence of inter-particle friction and damping on the dynamics of spherical projectile impacting onto a soil bed. Front Earth Sci 10:835271. https://doi.org/10.3389/feart.2022.835271
27. Guo J (2018) Exact solution for depth of impact crater into granular bed. J Eng Mech 144(1):06017018. https://doi.org/10.1061
28. Tiwari M, Mohan TK, Sen S (2014) Drag-force regimes in granular impact. Phys Rev E 90(6):062202. https://doi.org/10.1103/PhysRevE.90.062202
29. Tsimring LS, Volfson D (2005) Modeling of impact cratering in granular media. Powders and grains 2:1215–1223
30. Brzinski TA III, Mayor P, Durian DJ (2013) Depth-dependent resistance of granular media to vertical penetration. Phys Rev Lett 111(16):168002. https://doi.org/10.1103/PhysRevLett.111.168002
31. Hill G, Yeung S, Koehler SA (2005) Scaling vertical drag forces in granular media. EPL (Europhysics Letters) 72(1):137. https://doi.org/10.1209/epl/i2005-10203-3
32. Clark AH, Behringer RP (2013) Granular impact model as an energy-depth relation. EPL (Europhysics Letters) 101(6):64001. https://doi.org/10.1209/0295-5075/101/64001
33. Bester CS, Behringer RP (2017) Collisional model of energy dissipation in three-dimensional granular impact. Phys Rev E 95(3):032906. https://doi.org/10.1103/PhysRevE.95.032906
34. Mishra BK, Rajamani RK (1992) The discrete element method for the simulation of ball mills. Appl Math Model 16(11):598–604. https://doi.org/10.1016/0307-904X(92)90035-2
35. Wu CY, Cocks AC, Gillia OT, Thompson DA (2003) Experimental and numerical investigations of powder transfer. Powder Technol 138(2–3):216–228. https://doi.org/10.1016/j.powtec.2003.09.011
36. Cundall PA, Strack OD (1979) A discrete numerical model for granular assemblies. Geotechnique 29(1):47–65. https://doi.org/10.1680/geot.1979.29.1.47
37. Ghaboussi J, Barbosa R (1990) Three-dimensional discrete element method for granular materials. Int J Numer Anal Meth Geomech 14(7):451–472. https://doi.org/10.1002/nag.1610140702
38. Albert R, Pfeifer MA, Barabási AL, Schiffer P (1999) Slow drag in a granular medium. Phys Rev Lett 82(1):205. https://doi.org/10.1103/PhysRevLett.82.205
39. Van Der Meer D (2017) Impact on granular beds. Annu Rev Fluid Mech 49:463–484. https://doi.org/10.1146/annurev-fluid-010816-060213
40. Kang W, Feng Y, Liu C, Blumenfeld R (2018) Archimedes' law explains penetration of solids into granular media. Nat Commun 9(1):1–9. https://doi.org/10.1038/s41467-018-03344-3
41. Moghisi M, Squire PT (1981) An experimental investigation of the initial force of impact on a sphere striking a liquid surface. J Fluid Mech 108:133–146. https://doi.org/10.1017/S0022112081002036